Chapter 4

Elastic Properties of Bone Lamellae with Fibrillar Orientation

4.1 Introduction

Bone is a fibrous composite, of which lamellar bone is the most abundant type in many mammals, including humans. Its characteristic building block is known as the bone lamella, which is stacked at different orientations to form a laminated structure. While the microstructure of cancellous bone, known as trabecular pockets, is composed of irregular, sinuous lamellae, the microstructure of cortical bone is formed by regular, cylindrical shaped lamellae [4], which arrange around haversian channels forming osteons. A lamella at an observation scale of several μm is composed of mineralized collagen fibrils embedded in extrafibrillar mineral foam [5]. In 1906, Gebhardt [6] categorized the differences between lamellar types in terms of the orientation of their higher percentage components and proposed that collagen fibrils change orientation from one lamella to the next. In the 1960s, Ascenzi A. and collaborators introduced three basic types of osteons with lamellae having marked transversal, alternative, and longitudinal fibril orientations, which appeared as bright, alternating or dark in cross section under polarized light microscopy [7, 8].

More recently, Giraud-Guille [9] proposed, through transmitted electron microscopy, the so-called orthogonal plywood and the twisted plywood model. For the orthogonal plywood model, the orientation of collagen fibrils changes from one lamella

to the next by an angle close to 90°. The latter model possesses a continuous rotation of collagen fibrils from one layer to the next, which refines Gebhardt's model and explains the ability of the osteon to resist stresses along a large range of directions. Weiner et al. [10, 11] proposed the five sublayer model of a lamellar unit in which each sublayer is an array of aligned mineralized collagen fibrils with a progressive rotation of about 30°. The thicknesses of the five sublayers differ with two of them being thicker, which reflects the thickness distribution observed in rat and baboon bones. Wagermaier et al. [3] reconstructed the three-dimensional orientation of the mineralized collagen fibrils within a single lamella using scanning x-ray diffraction with a micron-sized synchrotron beam, along with measurements of local mineral crystallographic axis directions. In this way, the fibril orientations, beginning from the center of the osteon to the outmost lamella, were measured with a resolution of 1 μm. Ascenzi and Lomovtsev [1] used scanning confocal microscopy to quantify fibril orientations by location within the lamellar thickness. Using their method, the orientation patterns of the so-called extinct and bright lamellae were obtained.

Experimental measurements of the elastic properties at the length scale of a bone lamella are possible by means of acoustic impedance measurements and nanoindentation [12]. In 2009, Franzoso and Zysset [2] performed nanoindentation on osteons in two orthogonal directions. Their experimental indentation moduli varied with indentation direction and showed a noticeable anisotropy.

There are several mechanical models that have been proposed to estimate the elastic constants of bone at the ultrastructural level. Pidaparti et al. [13] built a simple

composite model for osteon bone based on experimental data using a modified rule-of-mixtures theory. Their model fit the experimental data best when the collagen was aligned 30° from the long axis of the bone. Akiva et al. [14] modeled each layer of a lamellar unit as a unidirectional plane-parallel platelet reinforced composite and then assembled them in different orientations using the mixture rule. Jasiuk and Ostoja-Starzewski [15] used a finite element model, which included a spatially random network of collagen fibrils to simulate a single lamella as a function of fibril volume fraction. Hellmich et al. [5, 16] utilized a multiscale homogenization scheme to deliver effective elastic properties of bone materials at different scales. Yoon and Cowin [17] introduced three distinct and organized hierarchical levels to represent a single bone lamella. Reisinger et al. [18] combined a finite element unit cell method with a homogenized scheme to account for different fibril orientation patterns in the lamellae.

In this chapter, we aim to understand the effect of collagen fibril orientations on the elastic properties of bone lamellae or lamellar units. Their effective anisotropic linear elastic properties are calculated based on the multiscale homogenized model developed in Chapter 3 combined with a micromechanical framework of layered composite and fibril orientation patterns observed in experiments. The resulting effective properties are then compared with the nanoindentation experimental results in two orthogonal directions.

4.2 Methods

In the framework of micromechanics, the effective properties of the laminated composite model of the lamellar unit as shown in **Figure 4-1**, which has a specific fibril orientation distribution pattern in each layer, can be obtained through a hierarchical approach. First, the effective properties of each layer are evaluated using the method developed in Chapter 3. Subsequently, the effective properties of the laminated composite were estimated by assuming that each layer is a homogeneous solid.

4.2.1 Ultrastructure (Homogenization of Single Layer)

At the ultrastructural scale, mineralized collagen fibrils are present in bundles and embedded as inclusions into the extrafibrillar mineral foam, which is composed of hydroxyapatite, ultrastructural water and non-collageneous proteins (cf. **Figure 4-2**). The volume fraction of the mineralized collagen fibrils is denoted as ϕ_{fib}. By using a Ju-Chen first order micromechanical approximation [19, 20] and performing orientation averaging procedures (cf. **Appendix II**), the effective properties of ultrastructure, $\boldsymbol{C}_{ultra}$, can be expressed as

$$\boldsymbol{C}_{ultra} = \boldsymbol{C}_{ef} \bullet \left(\boldsymbol{I} + \phi_{fib} \boldsymbol{\Omega} \bullet \boldsymbol{\Lambda}^{-1} \right) \tag{4.1}$$

The fourth-rank tensor $\boldsymbol{\Omega}$ and $\boldsymbol{\Lambda}$ can be written as

$$\Lambda_{ijkl} = I_{ijkl} - \phi_{fib} \int_0^{2\pi} Q_{mi} Q_{nj} S_{mnpq} \left(S_{pqst} + A_{pqst} \right)^{-1} Q_{sk} Q_{tl} P(\theta) d\theta \tag{4.2}$$

$$\Omega_{ijkl} = \int_0^{2\pi} Q_{mi} Q_{nj} \left(S_{mnpq} + A_{mnpq} \right)^{-1} Q_{pk} Q_{ql} P(\theta) d\theta \tag{4.3}$$

where $\boldsymbol{I}$ signifies the fourth-rank identity tensor, $\boldsymbol{S}$ is the Eshelby's tensor for the spheroid, $P(\theta)$ represents the probability density function of the orientation, Q is the transformation matrix with the following form,

$$[Q_{ij}] = \begin{bmatrix} 1 & 0 & 0 \\ 0 & \cos\theta & \sin\theta \\ 0 & -\sin\theta & \cos\theta \end{bmatrix} \tag{4.4}$$

and

$$\boldsymbol{A} = \left(\boldsymbol{C}_{fib} - \boldsymbol{C}_{ef}\right)^{-1} \bullet \boldsymbol{C}_{ef} \tag{4.5}$$

The parameters used in the model are listed in **Table 4-1** and are consistent with average human lamellar bone.

4.2.2 Multilayer Composite Model

Let us consider a laminated composite in which the bonding between the layers is assumed perfect, i.e. the displacement and tractions across the interfaces are continuous. Furthermore, the thickness of each layer is assumed to be much greater than the fiber diameter so that the effective properties of the laminated composite can be obtained through the hierarchical approach we proposed.

By introducing the following expressions [21],

$$\boldsymbol{\sigma}_n = \begin{bmatrix} \sigma_{11} \\ \sigma_{13} \\ \sigma_{12} \end{bmatrix}, \quad \boldsymbol{\sigma}_t = \begin{bmatrix} \sigma_{22} \\ \sigma_{33} \\ \sigma_{23} \end{bmatrix}, \quad \boldsymbol{\varepsilon}_n = \begin{bmatrix} \varepsilon_{11} \\ 2\varepsilon_{13} \\ 2\varepsilon_{12} \end{bmatrix}, \quad \boldsymbol{\varepsilon}_t = \begin{bmatrix} \varepsilon_{22} \\ \varepsilon_{33} \\ 2\varepsilon_{23} \end{bmatrix} \tag{4.6}$$

we can rewrite the stress-strain relation using Voigt notation as

$$\boldsymbol{\sigma}_n = \boldsymbol{C}_{nn}\boldsymbol{\varepsilon}_n + \boldsymbol{C}_{nt}\boldsymbol{\varepsilon}_t$$
$$\boldsymbol{\sigma}_t = \boldsymbol{C}_{tn}\boldsymbol{\varepsilon}_n + \boldsymbol{C}_{tt}\boldsymbol{\varepsilon}_t \tag{4.7}$$

where

$$\boldsymbol{C}_{nn} = \begin{bmatrix} C_{11} & C_{15} & C_{16} \\ C_{15} & C_{55} & C_{56} \\ C_{16} & C_{56} & C_{66} \end{bmatrix}, \qquad \boldsymbol{C}_{nt} = \begin{bmatrix} C_{12} & C_{13} & C_{14} \\ C_{25} & C_{35} & C_{45} \\ C_{26} & C_{36} & C_{46} \end{bmatrix} \tag{4.8}$$

$$\boldsymbol{C}_{tn} = \begin{bmatrix} C_{12} & C_{25} & C_{26} \\ C_{13} & C_{35} & C_{36} \\ C_{14} & C_{45} & C_{46} \end{bmatrix}, \qquad \boldsymbol{C}_{tt} = \begin{bmatrix} C_{22} & C_{23} & C_{24} \\ C_{23} & C_{33} & C_{34} \\ C_{24} & C_{34} & C_{44} \end{bmatrix} \tag{4.9}$$

Consider a laminated composite consisting of N layers of homogeneous materials as shown in **Figure 4-3**. Each layer is assumed to be homogeneous with its respective elastic property denoted by $\boldsymbol{C}^{(k)}$, $(k = 1, 2, \cdots N)$ in Voigt notation. Therefore, for the kth layer, the stress-strain relation follows from Eq. (4.7)

$$\boldsymbol{\sigma}_n^{(k)} = \boldsymbol{C}_{nn}^{(k)}\boldsymbol{\varepsilon}_n^{(k)} + \boldsymbol{C}_{nt}\boldsymbol{\varepsilon}_t^{(k)} \tag{4.10}$$

$$\boldsymbol{\sigma}_t^{(k)} = \boldsymbol{C}_{tn}^{(k)}\boldsymbol{\varepsilon}_n^{(k)} + \boldsymbol{C}_{tt}^{(k)}\boldsymbol{\varepsilon}_t^{(k)} \tag{4.11}$$

It is assumed here that the representative volume element being considered is under a uniform state of deformation. It is further assumed that the traction and displacements are continuous across the interfaces. Therefore, we arrive at

$$\boldsymbol{\sigma}_n^{(k)} = \boldsymbol{\sigma}_n, \quad \boldsymbol{\varepsilon}_t^{(k)} = \boldsymbol{\varepsilon}_t \quad \text{for } k = 1,\ 2, \cdots, N \tag{4.12}$$

Substituting Eq. (4.12) into Eq. (4.10) yields

$$\boldsymbol{\varepsilon}_n^{(k)} = \left(\boldsymbol{C}_{nn}^{(k)}\right)^{-1}\left(\boldsymbol{\sigma}_n - \boldsymbol{C}_{nt}^{(k)}\boldsymbol{\varepsilon}_t^{(k)}\right) \tag{4.13}$$

Taking the average of $\boldsymbol{\varepsilon}_n^{(k)}$ over the representative volume element results in

$$
\begin{aligned}
\boldsymbol{\varepsilon}_n &= \sum_{k=1}^{N} \phi^{(k)} \boldsymbol{\varepsilon}_n^{(k)} \\
&= \sum_{k=1}^{N} \phi^{(k)} \left(\boldsymbol{C}_{nn}^{(k)} \right)^{-1} \boldsymbol{\sigma}_n - \sum_{k=1}^{N} \phi^{(k)} \left(\boldsymbol{C}_{nn}^{(k)} \right)^{-1} \boldsymbol{C}_{nt}^{(k)} \boldsymbol{\varepsilon}_t^{(k)}
\end{aligned} \tag{4.14}
$$

where $\phi^{(k)}$ is the volume fraction of the kth layer. By rearranging Eq. (4.14), we have

$$
\boldsymbol{\sigma}_n = \boldsymbol{C}_{nn}^{*} \varepsilon_n \; + \; \boldsymbol{C}_{nt}^{*} \varepsilon_t \tag{4.15}
$$

where

$$
\boldsymbol{C}_{nn}^{*} = \left[\sum_{k=1}^{N} \phi^{(k)} \left(\boldsymbol{C}_{nn}^{(k)} \right)^{-1} \right]^{-1} \tag{4.16}
$$

$$
\boldsymbol{C}_{nt}^{*} = \boldsymbol{C}_{nn}^{*} \left[\sum_{k=1}^{N} \phi^{(k)} \left(\boldsymbol{C}_{nn}^{(k)} \right)^{-1} \boldsymbol{C}_{nt}^{(k)} \right] \tag{4.17}
$$

Next, substituting Eq. (4.13) into Eq. (4.11) results in

$$
\begin{aligned}
\boldsymbol{\sigma}_t^{(k)} &= \boldsymbol{C}_{tn}^{(k)} \left(\boldsymbol{C}_{nn}^{(k)} \right)^{-1} \left(\boldsymbol{\sigma}_n - \boldsymbol{C}_{nt}^{(k)} : \boldsymbol{\varepsilon}_t^{(k)} \right) + \boldsymbol{C}_{tt}^{(k)} \boldsymbol{\varepsilon}_t \\
&= \boldsymbol{C}_{tn}^{(k)} \left(\boldsymbol{C}_{nn}^{(k)} \right)^{-1} \boldsymbol{\sigma}_n + \left[\boldsymbol{C}_{tt}^{(k)} - \boldsymbol{C}_{tn}^{(k)} \left(\boldsymbol{C}_{nn}^{(k)} \right)^{-1} \boldsymbol{C}_{nt}^{(k)} \right] \boldsymbol{\varepsilon}_t
\end{aligned} \tag{4.18}
$$

Taking the average of $\boldsymbol{\sigma}_t^{(k)}$ over the representative volume element leads to

$$
\begin{aligned}
\boldsymbol{\sigma}_t &= \sum_{k=1}^{N} \phi^{(k)} \boldsymbol{\sigma}_t^{(k)} \\
&= \sum_{k=1}^{N} \phi^{(k)} \boldsymbol{C}_{tn}^{(k)} \left(\boldsymbol{C}_{nn}^{(k)} \right)^{-1} \boldsymbol{\sigma}_n + \sum_{k=1}^{N} \phi^{(k)} \left[\boldsymbol{C}_{tt}^{(k)} - \boldsymbol{C}_{tn}^{(k)} \left(\boldsymbol{C}_{nn}^{(k)} \right)^{-1} \boldsymbol{C}_{nt}^{(k)} \right] \boldsymbol{\varepsilon}_t
\end{aligned} \tag{4.19}
$$

Substituting Eq. (4.15) into Eq. (4.19) yields

$$
\boldsymbol{\sigma}_t = \boldsymbol{C}_{tn}^{*} \boldsymbol{\varepsilon}_n + \boldsymbol{C}_{nn}^{*} \boldsymbol{\varepsilon}_t \tag{4.20}
$$

where

$$
\boldsymbol{C}_{tn}^{*} = \left[\sum_{k=1}^{N} \phi^{(k)} \boldsymbol{C}_{tn}^{(k)} \left(\boldsymbol{C}_{nn}^{(k)} \right)^{-1} \right] \boldsymbol{C}_{nn}^{*} \tag{4.21}
$$

$$\boldsymbol{C}_{tt}^{*} = \sum_{k=1}^{N} \boldsymbol{\phi}^{(k)} \boldsymbol{C}_{tt}^{(k)} + \sum_{k=1}^{N} \boldsymbol{\phi}^{(k)} \boldsymbol{C}_{tn}^{(k)} \left(\boldsymbol{C}_{nn}^{(k)} \right)^{-1} \left(\boldsymbol{C}_{nt}^{*} - \boldsymbol{C}_{nt}^{(k)} \right) \tag{4.22}$$

The complete effective Voigt elastic properties of the laminated composite can be obtained by combing equations (4.16), (4.17), (4.21) and (4.22).

4.3 Numerical Simulations

The stiffness values of the lamellar units are predicted using the proposed hierarchical approach for five different fibril orientation patterns proposed or observed in experiments by other researchers. The Young's modulus for arbitrary directions in the $x_2 - x_3$ plane, as well as their global ratio defined as E_2/E_3, are calculated and compared with the indentation modulus measured by Franzoso and Zysset [2] listed in **Table 4-2**. At the same time, the Young's modulus orthogonal to the plane of the lamellar units, E_1, is constant because it is not affected by the in-plane fibril orientation patterns.

4.3.1 Orthogonal plywood

The orthogonal plywood fibril orientation pattern proposed by Giraud-Guile [9] describes the bone lamella as parallel planes with only two alternating fibril directions: -45° and 45° along the x_3 axis (**Figure 4-4a**). The maximum stiffness clearly happens in the main fibril directions with an approximate value of 20.29 GPa (**Figure 4-4b**). Its global stiffness ratio is 1.0.

4.3.2 Twisted plywood

The twisted plywood fibril orientation pattern proposed by Giraud-Guile [9] defines the bone lamella as a stack of planes with fibril directions rotating continuously from one plane to the next by a constant angle. A rotation by 180° of fibrils corresponds to the periodicity of the lamellae (**Figure 4-5a**). The effective elastic properties of the twisted plywood lamella are therefore transversely isotropic (**Figure 4-5b**). Accordingly, the Young's moduli in the $x_2 - x_3$ plane are constant with an approximate value of 18.85 GPa. Its global stiffness ratio is also 1.0.

4.3.3 Five sublayer model

Weiner et al. [10, 11] proposed that lamellar bone should be viewed as a series of lamellar units, each of which is composed of five sublayers. The fibrils in successive sublayers rotate progressively by about 30° in one direction. In addition, the fourth and fifth sublayers are much thicker than the first, second, and third sublayers (**Figure 4-6a**, **Figure 4-7a**). The relative thicknesses of the sublayers may be adapted to different circumstances resulting in varied effective anisotropic elastic properties as shown in **Figure 4-6b** and **Figure 4-7b**. The maximum Young's moduli are 20.83 GPa and 22.87 GPa at 82.39° and 76.87° respectively. The global stiffness ratio falls between 1.20 and 1.39.

4.3.4 Orientation patterns of Wagermaier et al.

Using scanning small angle x-ray scattering (SAXS) and wide angle x-ray diffraction (WAXD) with a spatial resolution of 1μm, Wagermaier et al. [3] measured the local mineral crystallographic axis direction and reconstructed the three-dimensional orientation of the mineralized fibrils within a single osteon lamella (~5 μm). **Figure 4-8** shows the fibril orientation pattern from the most interior lamella in the osteon. While lamellae 1 to 7 seem to have periodic orientation patterns, the lamella 8 shows a different orientation than the others. However, the calculated effective elastic properties of all lamellae show similar orientations with maximum Young's moduli at $118.67 \pm 7.32^{\circ}$ in the $x_2 - x_3$ plane (**Figure 4-9**). The mean and the standard deviation of Young's moduli of all lamellae at their preferred orientations is 24.62±1.66 GPa. Furthermore, their average global stiffness ratios are 1.30±0.14.

4.3.5 Orientation patterns of Ascenzi and Lomovtsev

By application of confocal laser microscopy, paired with image analysis, Ascenzi and Lomovtsev [1] quantified fibril orientations by location within the lamellar thickness. The fibril orientation is classified as transverse ($0^{\circ} - 22.5^{\circ}$ and $157.5^{\circ} - 180^{\circ}$), oblique acute ($45^{\circ} \pm 22.5^{\circ}$), longitudinal ($90^{\circ} \pm 22.5^{\circ}$) and oblique obtuse ($135^{\circ} \pm 22.5^{\circ}$) in their study. Based on their observations, fibril orientation patterns for extinct and bright lamellae are shown in **Figure 4-10**. For extinct lamella, the maximum Young's modulus is 26.31 GPa and is oriented at 78.83°; the global stiffness ratio is approximately 1.76

(**Figure 4-11A**). For bright lamella, the maximum Young's modulus is 25.30 GPa and happens at a much smaller angle of 45.40°; its global stiffness ratio is also smaller with an approximate value of 1.02. If we consider a set of extinct and bright lamellae with equal thicknesses as a "lamellar unit", then its maximum Young's modulus is 24.07 GPa oriented at 64.77°, and its global stiffness ratio is around 1.34 (**Figure 4-12**).

4.4 Discussion

Generally, our numerical results are within the standard deviation range of the experimental indentation results from Franzoso and Zysset [2]. However, the immanent structures of orthogonal and twisted plywood fibril orientation patterns lead to a global stiffness ratio of exactly 1.0, which was not observed in the experiments.

The directions of the maximum Young's moduli of the fibril orientation patterns by Wagermaier et al. [3] and Ascenzi and Lomovtsev [1] are aligned on at average 28.67° and 25.23° respectively to the longitudinal direction of the osteon (**Figure 4-9** and **Figure 4-12**), which is consistent with the principle orientation of collagen investigated by Turner et al. [22].

The five sublayer model of Weiner et al. [10, 11] seems to be a good choice when the experimental measurements of fibril orientations are not available. Both the effective elastic properties and global stiffness ratio in the lamella plane are close to the experimental results. Furthermore, it is relatively simple to adjust relative thicknesses to fit the experimental data.

The presented hierarchical approach is a useful tool for studying the elastic behavior of lamellar bone. However, the effective elastic properties of the lamellae are affected by the lower level homogenization steps in which the calculated properties have not been validated by experiments.

4.5 Conclusion

Within the framework of micromechanics, we have predicted the effective anisotropic linear elastic properties of bone lamellae or lamellar units; these predictions are quite similar to reported experimental results. The effects of fibril orientation patterns on the elastic properties of lamellar bone were also investigated. The proposed framework can reasonably determine the effective elastic properties of lamellar bone based on the fibril orientation patterns observed in experiments.

Table 4-1. Set of input parameters for the ultrastructure

Parameters	**Values**	**Reference**
Collagen elastic modulus	2.9 GPa	Sasaki and Odajima [23]
Collagen Poisson's ratio	0.3	-
Apatite crystal bulk modulus	80 GPa	Gilmore and Katz [24]
Apatite crystal shear modulus	45 GPa	Gilmore and Katz [24]
Mineral crystal aspect ratio in fibril	40/3	Akkus [25]
Ultrastructural water and void aspect ratio	1	-
Fibril aspect ratio	100	-
Fibril volume fraction in ultrastructure	0.53	Fritsch and Hellmich [5, 16]
Apatite crystal volume fraction in ultrastructure	0.34	Raum et al. [26] Fritsch and Hellmich [5, 16]
Apatite crystal distribution parameter	0.75	Lees et al. [27] Sasaki et al. [28]

Table 4-2. Results of nanoindentation measurements

$E_{2,ind}$	$E_{3,ind}$	$E_{2,ind}/E_{3,ind}$	**Reference**
22.31 ± 2.16 GPa	18.06 ± 1.84 GPa	1.25 ± 0.18	Franzoso and Zysset [2]

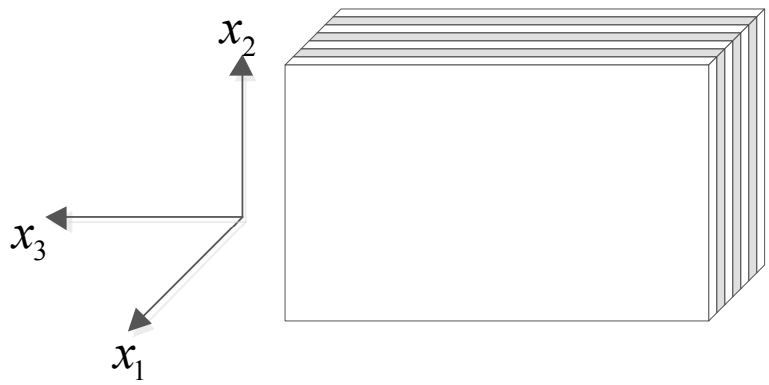

Figure 4-1. The proposed laminated composite model for lamellar unit. Each layer has specific fibril orientation distribution pattern.

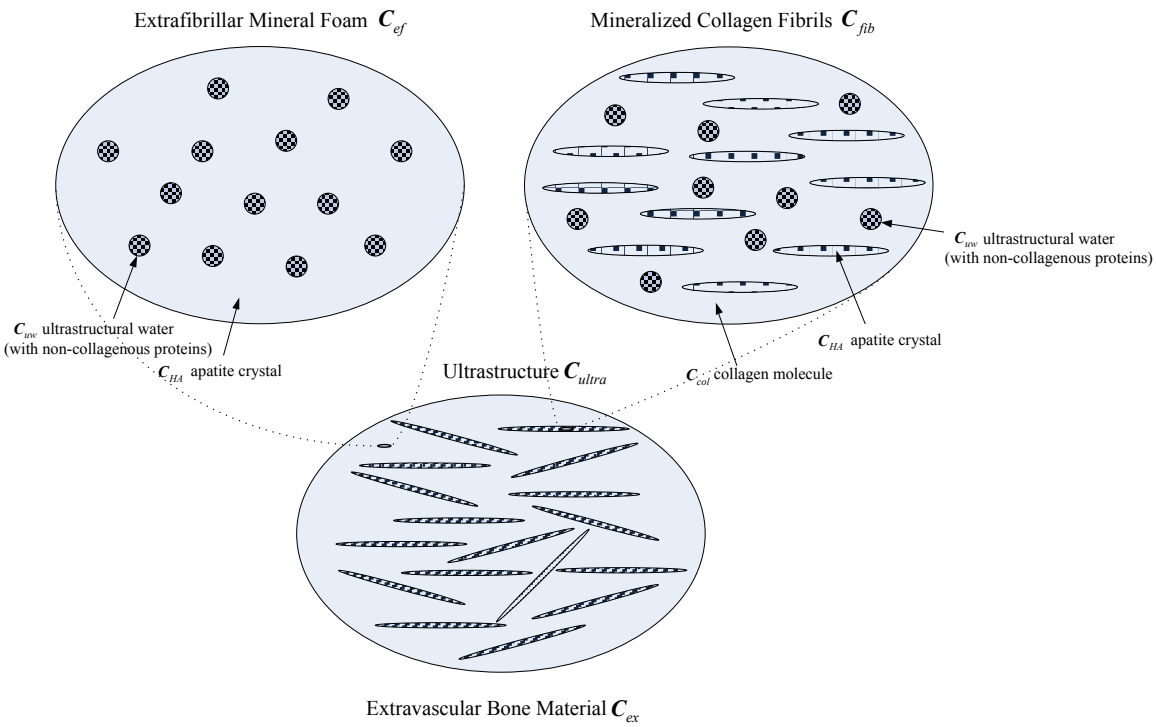

Figure 4-2. Micromechanical representation of ultrastructure based on three homogenization steps.

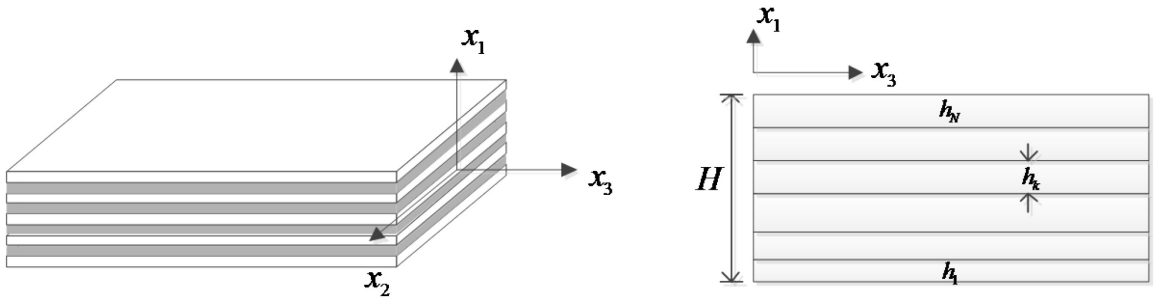

Figure 4-3. Multilayer composite.

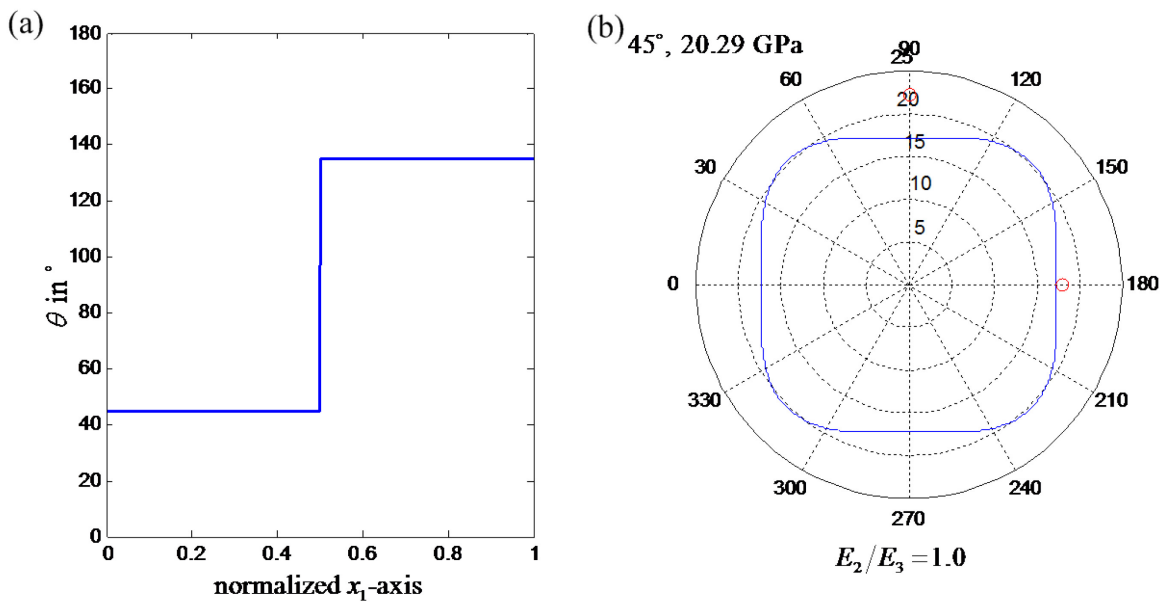

Figure 4-4. Results for the orthogonal plywood fibril orientation pattern: (a) Fibril angle θ depending on normalized $\boldsymbol{x_1}$-axis. (b) Young's modulus in the $\boldsymbol{x_2}-\boldsymbol{x_3}$ plane and its global ratio. The red circles represent the average values of the experimental indentation results from Franzoso and Zysset [2].

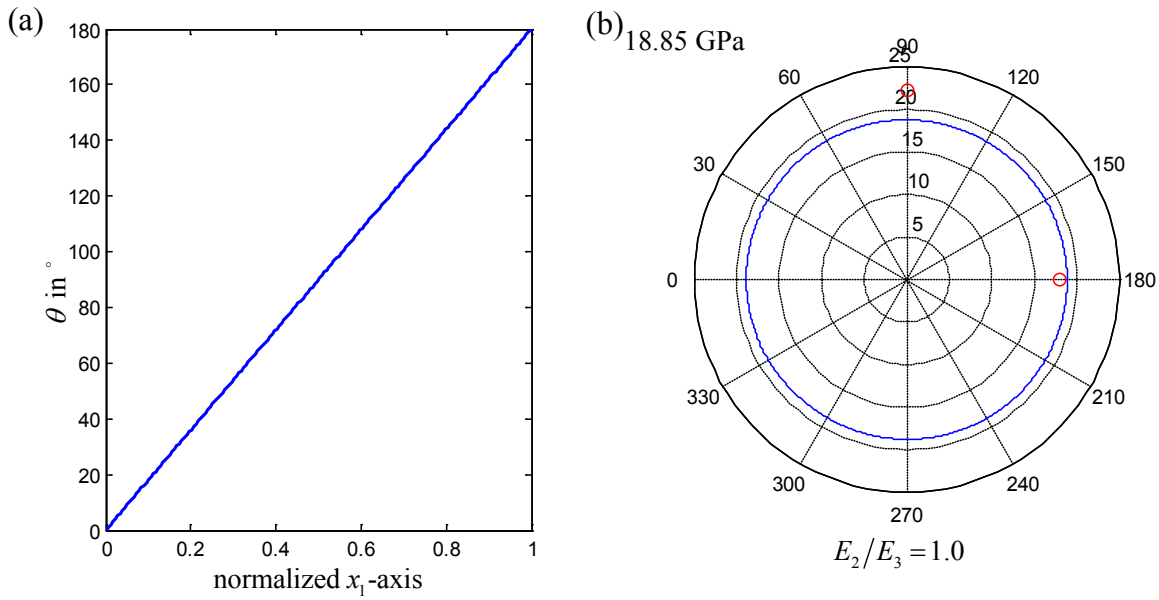

Figure 4-5. Results for the twisted plywood fibril orientation pattern: (a) Fibril angle θ depending on normalized $\boldsymbol{x_1}$-axis. (b) Young's modulus in the $\boldsymbol{x_2}-\boldsymbol{x_3}$ plane and its global ratio. The red circles represent the average values of the experimental indentation results from Franzoso and Zysset [2].

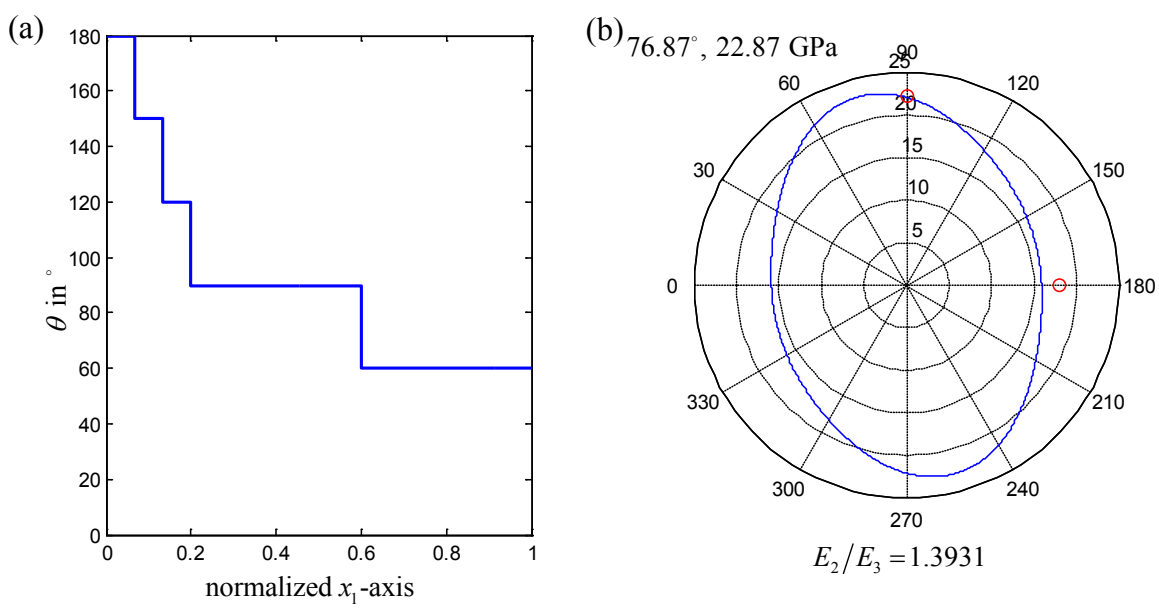

Figure 4-6. Results for the five sublayer model: (a) Fibril angle θ depending on normalized $\boldsymbol{x_1}$-axis. (b) Young's modulus in the $\boldsymbol{x_2}-\boldsymbol{x_3}$ plane and its global ratio. The red circles represent the average values of the experimental indentation results from Franzoso and Zysset [2].

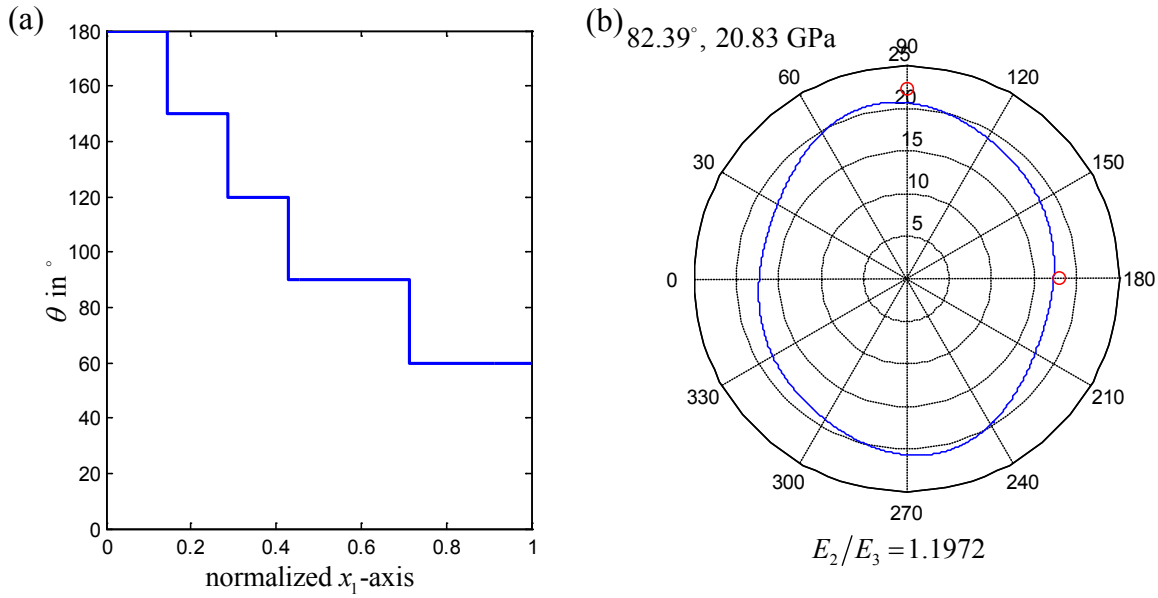

Figure 4-7. Results for the five sublayer model with different relative thicknesses: (a) Fibril angle θ depending on normalized $\boldsymbol{x_1}$-axis. (b) Young's modulus in the $\boldsymbol{x_2}-\boldsymbol{x_3}$ plane and its global ratio. The red circles represent the average values of the experimental indentation results from Franzoso and Zysset [2].

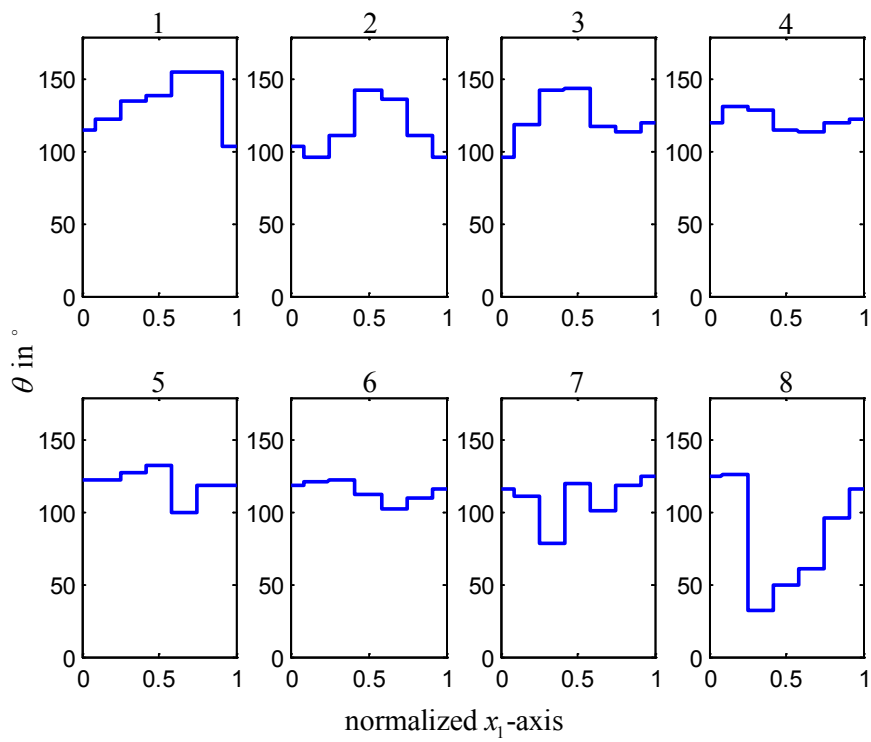

Figure 4-8. Fibril angle θ depending on normalized $\boldsymbol{x_1}$-axis from the most interior lamella [3].

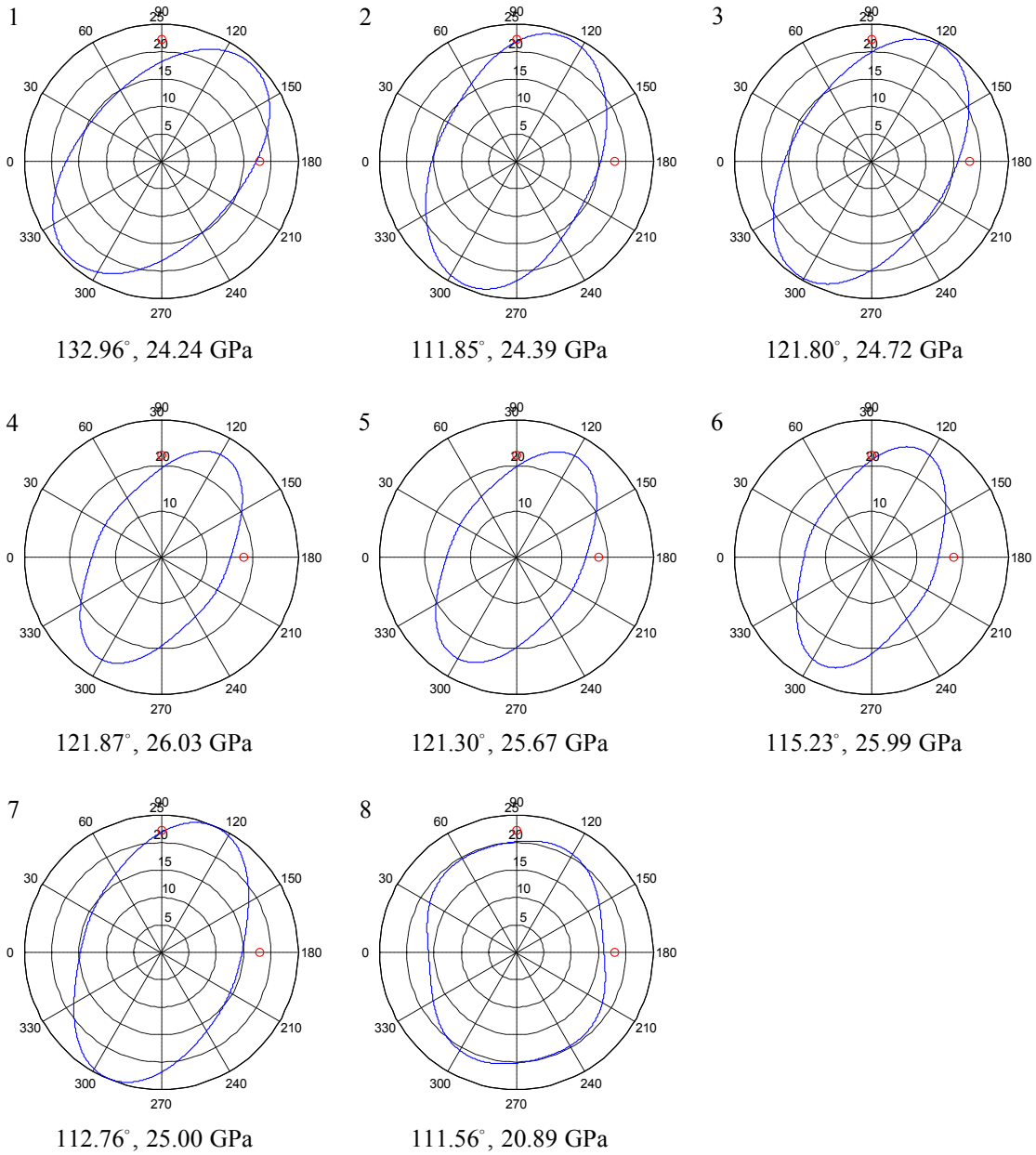

Figure 4-9. Results for the fibril orientation pattern of Wagermaier et al. [3] beginning from the most interior lamella 1 to 8. The red circles represent the average values of the experimental indentation results from Franzoso and Zysset [2].

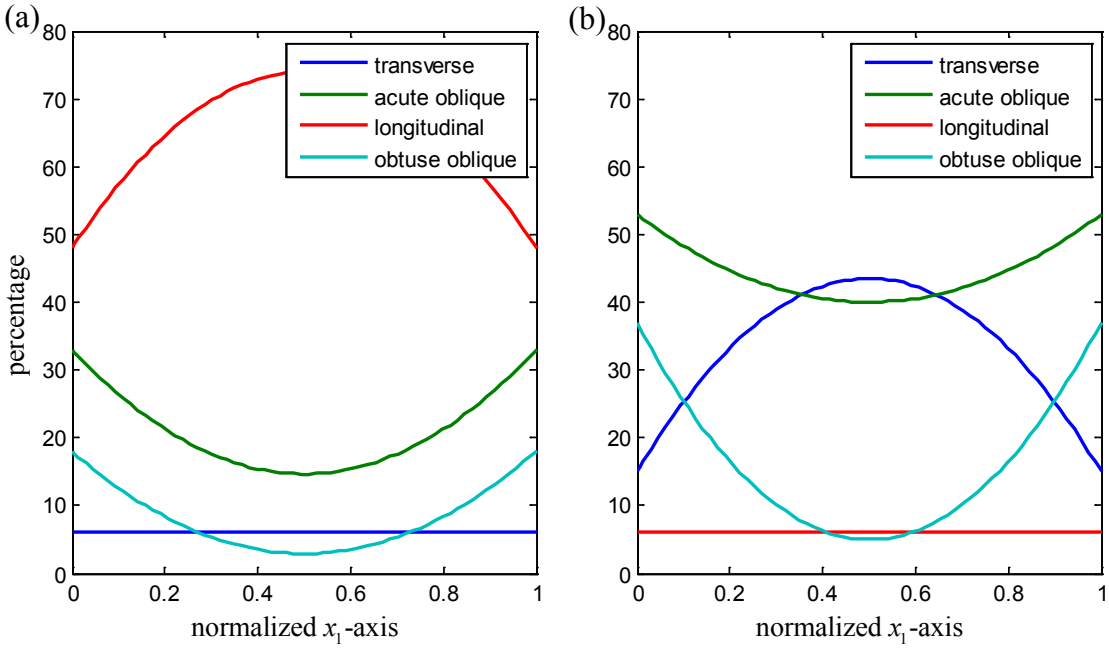

Figure 4-10. Percentages of fibril orientation through lamellar thickness for (a) extinct and (b) bright lamellae. Each of (a and b) shows three parabolas and a horizontal line.

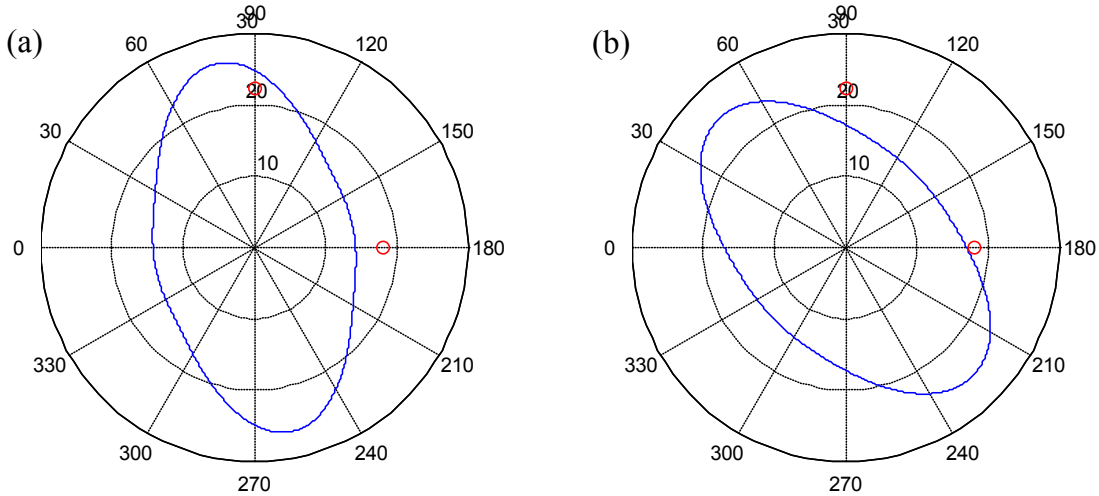

78.83°, 26.31 GPa

$E_2/E_3 = 1.7546$

45.40°, 25.30 GPa

$E_2/E_3 = 1.0164$

Figure 4-11. Results for the fibril orientation pattern of Ascenzi and Lomovtsev [1] for (a) extinct and (b) bright lamellae. The red circles represent the average values of the experimental indentation results from Franzoso and Zysset [2].

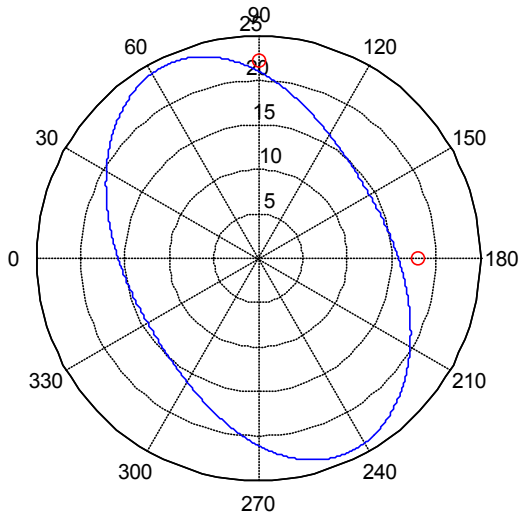

64.77°, 24.07 GPa

$E_2/E_3 = 1.3373$

Figure 4-12. Results for the fibril orientation pattern of Ascenzi and Lomovtsev [1] for a given "lamellar unit". The red circles represent the average values of the experimental indentation results from Franzoso and Zysset [2].

4.6 References

1. Ascenzi, M.-G. and A. Lomovtsev, *Collagen orientation patterns in human secondary osteons, quantified in the radial direction by confocal microscopy.* Journal of Structural Biology, 2006. **153**(1): p. 14-30.
2. Franzoso, G. and P.K. Zysset, *Elastic anisotropy of human cortical bone secondary osteons measured by nanoindentation.* Journal of Biomechanical Engineering, 2009. **131**(2): p. 021001-11.
3. Wagermaier, W., et al., *Spiral twisting of fiber orientation inside bone lamellae.* Biointerphases, 2006. **1**(1): p. 1-5.
4. Rho, J.-Y., L. Kuhn-Spearing, and P. Zioupos, *Mechanical properties and the hierarchical structure of bone.* Medical Engineering & Physics, 1998. **20**(2): p. 92-102.
5. Fritsch, A. and C. Hellmich, *`Universal' microstructural patterns in cortical and trabecular, extracellular and extravascular bone materials: Micromechanics-based prediction of anisotropic elasticity.* Journal of Theoretical Biology, 2007. **244**(4): p. 597-620.
6. Gebhardt, W., *Über funktionell wichtige Anordnungsweisen der feineren und gröberen Bauelemente des Wirbeltierknochens.* Development Genes and Evolution, 1905. **20**(2): p. 187-322.
7. Ascenzi, A. and E. Bonucci, *The tensile properties of single osteons.* The Anatomical Record, 1967. **158**(4): p. 375-386.

8. Ascenzi, A. and E. Bonucci, *The compressive properties of single osteons.* The Anatomical Record, 1968. **161**(3): p. 377-391.

9. Giraud-Guille, M.M., *Twisted plywood architecture of collagen fibrils in human compact bone osteons.* Calcif Tissue Int, 1988. **42**(3): p. 167-80.

10. Weiner, S., et al., *Rotated plywood structure of primary lamellar bone in the rat: Orientations of the collagen fibril arrays.* Bone, 1997. **20**(6): p. 509-514.

11. Weiner, S., W. Traub, and H.D. Wagner, *Lamellar Bone: Structure-Function Relations.* Journal of Structural Biology, 1999. **126**(3): p. 241-255.

12. Hofmann, T., et al., *Assessment of composition and anisotropic elastic properties of secondary osteon lamellae.* Journal of Biomechanics, 2006. **39**(12): p. 2282-2294.

13. Pidaparti, R.M.V., et al., *Bone mineral lies mainly outside collagen fibrils: Predictions of a composite model for osteonal bone.* Journal of biomechanics, 1996. **29**(7): p. 909-916.

14. Akiva, U., H.D. Wagner, and S. Weiner, *Modelling the three-dimensional elastic constants of parallel-fibred and lamellar bone.* Journal of Materials Science, 1998. **33**(6): p. 1497-1509.

15. Jasiuk, I. and M. Ostoja-Starzewski, *Modeling of bone at a single lamella level.* Biomechanics and Modeling in Mechanobiology, 2004. **3**(2): p. 67-74.

16. Hellmich, C., J.F. Barthelemy, and L. Dormieux, *Mineral-collagen interactions in elasticity of bone ultrastructure - a continuum micromechanics approach.* European Journal of Mechanics a-Solids, 2004. **23**(5): p. 783-810.

17. Yoon, Y. and S. Cowin, *The estimated elastic constants for a single bone osteonal lamella.* Biomechanics and Modeling in Mechanobiology, 2008. **7**(1): p. 1-11.

18. Reisinger, A., D. Pahr, and P. Zysset, *Elastic anisotropy of bone lamellae as a function of fibril orientation pattern.* Biomechanics and Modeling in Mechanobiology, 2011. **10**(1): p. 67-77.

19. Ju, J.W. and T.M. Chen, *Micromechanics and effective moduli of elastic composites containing randomly dispersed ellipsoidal inhomogeneities.* Acta Mechanica, 1994. **103**(1-4): p. 103-121.

20. Ju, J.W. and T.M. Chen, *Effective elastic moduli of two-phase composites containing randomly dispersed spherical inhomogeneities.* Acta Mechanica, 1994. **V103**(1): p. 123-144.

21. Qu, J. and M. Cherkaoui, *Fundamentals of micromechanics of solids*2006, Hoboken, N.J.: Wiley. xiii, 386 p.

22. Turner, C.H., A. Chandran, and R.M.V. Pidaparti, *The anisotropy of osteonal bone and its ultrastructural implications.* Bone, 1995. **17**(1): p. 85-89.

23. Sasaki, N. and S. Odajima, *Stress-strain curve and young's modulus of a collagen molecule as determined by the X-ray diffraction technique.* Journal of Biomechanics, 1996. **29**(5): p. 655-658.

24. Gilmore, R.S. and J.L. Katz, *Elastic properties of apatites.* Journal of Materials Science, 1982. **V17**(4): p. 1131-1141.

25. Akkus, O., *Elastic deformation of mineralized collagen fibrils: An equivalent inclusion based composite model.* Journal of Biomechanical Engineering-Transactions of the Asme, 2005. **127**(3): p. 383-390.

26. Raum, K. and et al., *Site-matched assessment of structural and tissue properties of cortical bone using scanning acoustic microscopy and synchrotron radiation μCT.* Physics in Medicine and Biology, 2006. **51**(3): p. 733.

27. Lees, S., et al., *The loci of mineral in turkey leg tendon as seen by atomic force microscope and electron microscopy.* Calcified Tissue International, 1994. **55**(3): p. 180-189.

28. Sasaki, N., et al., *Atomic force microscopic studies on the structure of bovine femoral cortical bone at the collagen fibril-mineral level.* Journal of Materials Science-Materials in Medicine, 2002. **13**(3): p. 333-337.